The published paper may be found at 10.1121/10.0004826

Reference for the published paper:
A. Aulitto, A. Hirschberg and I. Lopez Arteaga (2021) "Influence of geometry on acoustic end-corrections of slits in Microslit Absorbers". *Journal of the Acoustical Society of America*, Vol. 149(5) 3073.

Influence of geometry on acoustic end-corrections of slits in Microslit Absorbers

Alessia Aulitto[a)]

Department of Mechanical Engineering Dynamics and Control, Eindhoven University of Technology, P.O. Box 513, 5600 MB Eindhoven, The Netherlands

Avraham Hirschberg

Department of Applied Physics, Fluids and Flows, Eindhoven University of Technology, P.O. Box 513, 5600 MB Eindhoven, The Netherlands

and Ines Lopez Arteaga

Department of Mechanical Engineering Dynamics and Control, Eindhoven University of Technology, P.O. Box 513, 5600 MB Eindhoven, The Netherlands

[a)]e-mail: a.aulitto@tue.nl

Abstract

The acoustic behavior of individual slits within microslit absorbers (MSAs) is investigated to explore the influence of porosity, edge geometry, slit position and plate thickness. MSAs are plates with arrays of slit-shaped perforations, with the height of the order of the acoustic viscous boundary layer thickness, for optimized viscous dissipation. Due to hydrodynamic interaction, each slit behaves as confined in a rectangular channel. The flow within the slit is assumed to be incompressible. The viscous dissipation and the inertia are quantified by the resistive and the inertial end-corrections. These are estimated by using analytical results and numerical solutions of the Linearized Navier-Stokes equations. Expressions for the end-corrections are provided as functions of the ratio of the slit height to viscous boundary layer thickness (Shear number) and of the porosity. The inertial end-correction is sensitive to the far-field behavior of the flow and for low porosities strongly depends on the porosity, unlike for circular perforations. The resistive end-correction is dominated by the edge geometry of the perforation. The relative position of the slit with respect to the wall of the channel is important for distances to the wall of the order of the slit height. The plate thickness does not have a significant effect on the end-corrections.

I. INTRODUCTION

Microslit absorbers and plates (MSAs, MSPs) have been proposed by Maa[1] as sound absorbers at low frequencies, providing light-weight and compact solutions to substitute conventional materials, such as absorptive foams and porous structures. In simple MSAs the plate, consisting of an array of slit-like perforations, is mounted with a shallow or sub-partitioned backing cavity. Alternative designs of MSAs have been recently reported in the literature[2,3,4,5]. MSAs have several advantages with respect to micro-perforated plates (MPPs) with circular perforations. Using slits one can easily obtain a relatively large porosity, resulting in a higher Helmholtz resonance frequency, when needed. For equal porosity, a single slit replaces a large number of circular perforations. Furthermore, a slit can be used to delimit flexible structures whose vibration can contribute to the sound absorption[4,5]. Compared to the literature for circular perforations, fewer publications investigate the acoustic properties of slit-like perforations. Maa[1] states that no theory is available to predict inertial end-correction. The same viscous dissipation as for circular perforations is assumed. In the work of Maa[1], radiation to free space is assumed for each slit. The inertial end-correction model fails. This failure is solved when taking the confinement into account which is a consequence of the hydrodynamic interaction between slits. Ingard[6] obtained a solution for high Shear numbers, assuming a uniform flow in the slit and matching the resulting rigid piston oscillation model to a modal expansion of the flow in the confinement channel. Correct expressions for the inertial end-corrections, without typos, are presented by Jaouen *et al.*[7]. The same model is used by Vigran[9]. Another model, based on a locally incompressible potential flow with a thin boundary layer, is proposed by Morse and Ingard[8], for an abrupt transition with sharp square edges. This model yields both inertial and resistive end-corrections in the limit of high Shear numbers. For a slit in an infinitely thin plate, the same approach does predict an inertial end-correction. However, the singularity of the potential flow at the edge of an infinitely thin plate results in a divergence of the resistive end-correction. Morse and Ingard[8] propose to introduce a finite plate thickness to avoid this problem. The divergence of the resistive end-correction due to the singularity, at the edge of an infinitely thin plate, suggests that the viscous dissipation is a local effect, strongly influenced by the edge geometry. Recent studies on circular perforations by Temiz *et al.*[13] and by Billard *et al.*[10] confirm the importance of edges on the viscous dissipation. One concludes that there is a lack of a complete model to describe the acoustic behavior of slits. For instance, both Ruiz *et al.*[11] and Cobo *et al.*[12] state that all the models proposed in literature do not fit experimental absorption curves of MSPs. Therefore, the goal of the present work is to complement the theoretical knowledge concerning the acoustical properties of microslits. In particular two effects appear to be ignored in the literature for slits: the influence of the position of the slit within the confinement channel and the influence of the edge shape. For a circular perforation, Temiz *et al.*[13] observed that chamfering the edges reduces the effective plate thickness

t_{eff} by a length of the order of the total length of the chamfers. A non-symmetric position of the slit within the confinement channel can be found when the periodicity of the array is not perfect or in the case of a sub-partitioned back cavity. In the present work, a combination of analytical models and numerical solutions of the incompressible Linearized-Navier Stokes equations is proposed. In Sec. II, two-dimensional analytical models are developed. In Sec. III, the numerical models and solutions of the incompressible Linearized Navier-Stokes equations (LNSE) using Comsol[14] v5.5 are described. In Sec. IV, analytical and numerical results are compared. Findings are summarized in Sec. V.

II. THEORY

A. Definition of the problem

Microslit plates (MSPs) are plates with arrays of slit-like perforations with height b in the sub-millimeter range and width $w >> b$. The plate thickness t_p is of the order of magnitude of the slit height. The acoustic properties of MSPs are defined by the porosity $\Phi = b/a$, with a the distance between neighboring slits. The hydrodynamical interaction between neighboring slits in the array can be described by considering a single slit of height b, confined within a channel of height a of rectangular cross-section aw given by the distance a between neighboring slits and the lateral width w of the slit. At the open front side of the MSA, the confinement channel represents the hydrodynamic interaction between neighboring slits. The confinement channel on the cavity side is resulting from physical walls in the case of a sub-partitioned cavity or is due to hydro-dynamical interactions. As illustrated in Fig.

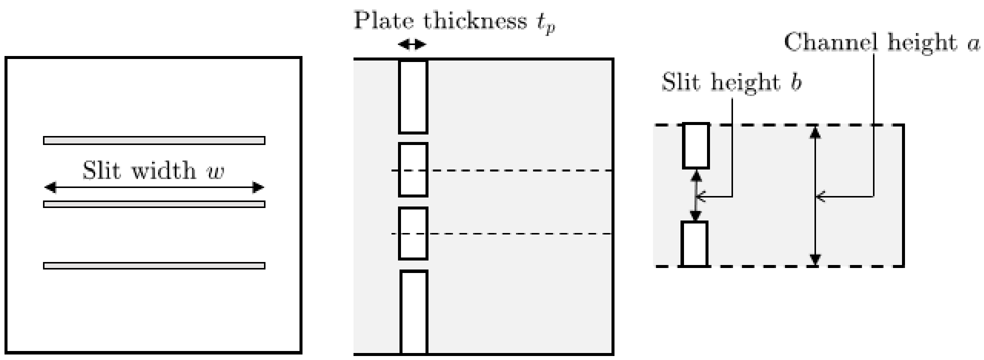

Figure 1: On the left, frontal view of the microslit plate with slit width w. In the middle, lateral view of the microslit plate of thickness t_p with back cavity. On the right, a single slit of height b with confinement channel of height a due to hydrodynamic interactions.

1, for a periodic array of slits, the confinement channel is placed symmetrically with respect to the slit. Assuming a long slit ($w >> b$) implies that one can consider a two-dimensional ($2D$) acoustical flow through the slit. As the slit forms the neck of a Helmholtz resonator with a portion of the back cavity as volume, the flow within the slit can be considered as locally incompressible up to the first resonance frequency of the resonator, $\omega_H = c\sqrt{\Phi/(d_c t_{eff})}$, with c the speed of sound, d_c the back cavity depth and t_{eff} the effective neck length. In the audio range, the square of the Helmholtz number is small,*i.e.* $He^2 = \left(\frac{\omega b}{c}\right)^2 < 10^{-1}$. Thermal effects in the slit are neglected. In the configuration in Fig. 1, thermal effects appear on the solid back wall and the front and back sides of the plate. In the confinement channel, the viscous and thermal effects are of the same order of magnitude. The viscous dissipation per unit surface in the perforation increases quadratically with the inverse of the porosity because the velocity increases as the inverse of the porosity and the dissipation is quadratic in the velocity. The temperature fluctuations and thermal dissipation in the perforations are (per unit surface) of the same order of magnitude as that in the confinement channel. Therefore viscous dissipation is in the perforation a factor $(1/\Phi)^2$ larger than thermal dissipation. Thermal effects within the perforations are negligible compared to those on the back wall and on the surface of the plate, because of the small porosity[10]. The thermal dissipation on the back wall and on the two sides of the perforated plate appears to be negligible compared to the viscous dissipation in the pore (for sufficiently small porosities) as demonstrated by Billard *et al.*[10]. The thermal boundary layer is described by the classical high Shear number model of Landau and Lifchitz[15]. The discussion is limited to the normal incidence of acoustic waves. One can describe the transition between the slit and the confinement channel by assuming over the plate thickness t_p an ideal 2D parallel flow for a long slit of height b extended over a so-called end-correction length. The extrapolation of the linear dependency of the acoustic pressure as a function of the distance from the slit opening in both the slit and the confinement channel is used to define the end-corrections. There is a resistive end-correction δ_{res} and an inertial end-correction δ_{in} corresponding to the pressure components $Re[\hat{p}]$ and

$Im[\hat{p}]$, respectively in phase with the volume flow oscillation $\hat{U}exp(i\omega t)$ and in phase with the time derivative of the volume flow oscillation. The inertial end-correction determines the Helmholtz resonance frequency, as shown in Zielinski *et al.*[5]. Assuming the same geometry on the front and backside of the plate, the effective neck length of the perforation is given by $t_{eff} = t_p + 2\delta_{in}$. The resistive end-correction takes into account the viscous dissipation and influences the quality factor of the Helmholtz resonance. To optimize viscous dissipation, the slit height is chosen to be of the order of magnitude of the acoustical viscous boundary layer thickness $\delta_v = \sqrt{2\nu/\omega}$, where ν is the kinematic viscosity of air and $\omega = 2\pi f$, with f the frequency. Hence, for typical applications, the Shear number $Sh_b = b/\delta_v$ is of order unity. The range $0.05 < Sh_b < 20$ is considered. As the plate thickness and end-corrections in MSPs are both typically of the order of the slit height, it is important to obtain an accurate prediction of end-corrections to design the absorbers.

B. Parallel flow

An analytical model for the flow in a long slit of height b is used as a reference to define the end-corrections and to define low and high Shear number limits. It is also used to assess the accuracy of the numerical solution of the incompressible Linearized Navier-Stokes equations. At low Helmholtz numbers ($He^2 = (\omega b/c)^2 << 1$), in absence of main flow, the acoustic field is considered as incompressible and is described by the equation of continuity

$$\nabla \cdot \vec{v} = 0 \tag{1}$$

and the linearized equation of motion

$$\rho \frac{\partial \vec{v}}{\partial t} = -\nabla p + \eta \nabla^2 \vec{v}, \tag{2}$$

where $\vec{v}$ is the velocity, p is the pressure fluctuation, ρ density of the air assumed to be uniform and constant and η is the dynamic viscosity. In a long thin slit of height b, width $w >> b$ and length $t_p >> b$, for $0 < x < t_p$ and $-b/2 < y < b/2$, the flow can be approximated by a 2D parallel flow $\vec{v} = (u(y,t), 0, 0)$. The continuity equation (Eq. 1) implies, in a two-dimensional parallel flow, that $\frac{\partial u}{\partial x} = 0$. Hence, the derivative with respect to x of the $x-$component of the equation of motion (Eq. 2) implies that $\frac{\partial^2 p}{\partial x^2} = 0$, *i.e.* the pressure is given by a linear function of the $x-$coordinate. The $y-$ and $z-$components of the equation of motion reduce to $\frac{\partial p}{\partial y} = \frac{\partial p}{\partial z} = 0$. This results in a uniform pressure in a cross-section of the slit. Consequently one has that $\frac{\partial p}{\partial x} = \Delta p / t_p$ with $\Delta p = p(t_p, t) - p(0, t)$. For a harmonic oscillation $\Delta p = \Delta \widehat{p} e^{i\omega t}$ the flow profile satisfying the no-slip boundary condition $(u, v) = (0, 0)$ on the slit walls $y = \pm b/2$ is

$$u(x,t) = \widehat{u} e^{i\omega t} = -\frac{i}{\rho\omega} \frac{\Delta \widehat{p}}{t_p} \left[1 - \frac{\cosh\left(\frac{(1+i)}{\delta_v} y\right)}{\cosh\left(\frac{(1+i)}{2\delta_v} b\right)} \right] e^{i\omega t}. \tag{3}$$

The cross-sectional averaged amplitude of the velocity $< \widehat{u} >$ is

$$< \widehat{u} > = \frac{1}{b} \int_{-b/2}^{b/2} \widehat{u} dy = -\frac{i}{\rho\omega} \frac{\Delta \widehat{p}}{t_p} \cdot \left[1 - \frac{2}{(1+i) Sh_b} \tanh\left(\frac{(1+i)}{2} Sh_b \right) \right] e^{i\omega t}, \tag{4}$$

with $Sh_b = b/\delta_v$, the Shear number. The slit impedance Z_b is defined as by Morse and Ingard[8]:

$$Z_b = \frac{\Delta \widehat{p}}{wb < \widehat{u} >}. \tag{5}$$

At low Shear numbers $Sh_b < 1$, one can use the approximation

$$Z_b \approx \frac{12\eta t_p}{(wb)b^2} + i\frac{6}{5}\frac{\rho\omega t_p}{(wb)}. \tag{6}$$

One recognizes in the real part of Z_b the resistance corresponding to a parabolic flow (quasi-steady Poiseuille flow approximation). At high Shear numbers $Sh_b >> 1$, one has

$$Z_b \approx \frac{\rho\omega t_p}{(wb)Sh_b} + i\frac{\rho\omega t_p}{(wb)}\left(1 + \frac{1}{Sh_b}\right). \tag{7}$$

The first part of the imaginary part corresponds to the inertia of a uniform flow, which is a factor 6/5 lower than that of a parabolic flow (see Eq. 6). The time-averaged viscous dissipation $\bar{P}_W$ in the slit is given by Morse and Ingard[8]:

$$\bar{P}_W = \frac{1}{2} Re[Z_b] | < \widehat{u} > |^2 (wb)^2. \tag{8}$$

For $Sh_b >> 1$ using Eq. 7 one has

$$\bar{P}_W = \frac{1}{2}\rho\omega\delta_v | < \widehat{u} > |^2 w t_p. \tag{9}$$

This thin boundary layer approximation is used in Sec. II E for channels with non-uniform height. In this limit, the flow in the boundary layer is quasi-parallel along the wall. Therefore, one can use the dissipation per unit surface found in Eq. 9 when replacing $| < \widehat{u} > |$ by the amplitude of the tangential velocity $|\widehat{u}_{tan}|$ prevailing just outside the viscous boundary layer. Integration over the surface yields the total dissipation. This tangential velocity corresponds to that of a frictionless potential flow. This will be referred as the high Shear number limit or the thin boundary layer limit. Alternative derivations of this thin boundary layer equation are provided in literature[8, 17, 16, 18]. As explained by Morse and Ingard[8], this approximation fails for infinitely thin orifice plates. While Morse and Ingard[8] suggest that the approximation is valid for sharp square edges, the numerical integration of the Linearized Navier-Stokes equations will allow to verify this assumption.

C. Impedance and end-corrections

In this subsection a formal definition of impedance and end-corrections is provided. Consider the transition from a slit of height b to a channel of height $a > b$. In an ideal (reference) configuration the transition from the slit to the channel is abrupt: the flow can be described as a piece-wise parallel flow. In the actual flow, the transition from the slit to the channel is smooth. Far from the transition one can observe a linear change in the amplitude of the pressure as a function of the distance from the slit opening. This corresponds to a parallel flow in a slit of height b and in a confinement channel of height a. This far field can be extrapolated at each side of the transition towards the plate surface at $x = 0$ (slit opening). The complex pressure amplitude difference $\Delta\widehat{p}_t$ obtained across the transition by this extrapolation divided by volume flux amplitude $\widehat{U} =< \widehat{u} > bw$ is defined as the transition impedance Z_t. The inertial end-correction δ_{in} and the resistive end-correction δ_{res} are defined by:

$$\delta_{in} = \frac{Im\left[Z_t\right]}{Im\left[\frac{dZ_b}{dt_p}\right]}, \tag{10}$$

$$\delta_{res} = \frac{Re\left[Z_t\right]}{Re\left[\frac{dZ_b}{dt_p}\right]}. \tag{11}$$

The value of Z_b is calculated by combining Eq. 4 and Eq. 5. The resistive end-correction δ_{res} is in principle different from the inertial end-correction δ_{in}. In this work, the inertial and resistance end-correction of Morse and Ingard[8] will be used as reference. One has

$$Im[Z_{t,ref}] = \frac{\rho\omega}{\pi w}\left[\frac{(1-\Phi)^2}{2\Phi}\ln\frac{(1+\Phi)}{(1-\Phi)} + \ln\frac{(1+\Phi)^2}{4\Phi}\right], \tag{12}$$

$$Re[Z_{t,ref}] = \frac{\rho\omega}{2aSh_b w}(1-\Phi)\left[1+\frac{(1-\Phi^2)}{\pi\Phi}\ln\frac{(1+\Phi)}{(1-\Phi)}\right]. \tag{13}$$

The reference end-corrections, $\delta_{in,ref}$ and $\delta_{res,ref}$, can be calculated by replacing $Im[Z_{t,ref}]$ and $Re[Z_{t,ref}]$ in Eq.10 and Eq.11. For low porosity, the inertial end-corrections becomes $\delta_{in,limit}/b = (1-\ln(4\Phi))/\pi$. The inertial end-correction becomes infinitely large for vanishing porosity. This divergence can be avoided when taking into account the influence of the flow compressibility[19]. The resistive end-correction increases with decreasing porosity but reaches an asymptote $\delta_{res,limit}/b = (\pi+2)/(2\pi)$ for $\Phi \to 0$. In Fig. 2 values of the inertial and resistive end-corrections obtained from the literature for perforations with sharp edges are shown as function of the inverse of the porosity $1/\Phi = a/b$. Results for circular perforations are also displayed. A critical discussion of these data is provided by Kergomand and Garcia[20].

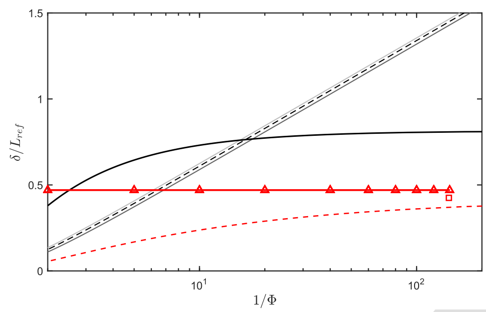

Figure 2: (Color online) Comparison of end-corrections for sharp-edged slit ($L_{ref} = b$) and circular perforation ($L_{ref} = d_p$) from the literature. Inertial end-corrections δ_{in} for slits (MSPs): - - - high Sh_b number limit for a slit in an infinitely thin plate[8], — Modal expansion of Ingard[6], — Thin boundary layer for square edged transition in channel[8]. — Resistive end-correction δ_{res} for square edged transition in channel[8]. - - - Inertial end-correction for circular perforations from Fok[21]. Resistive end-correction for circular perforations: □ from Temiz *et al.*[13] and −△ from Naderyan *et al.*[22].

The reference length L_{ref}, in Fig. 2 refers either to the height b for slits or to the perforation diameter d_p. It can be noted that the various results at high Sh_b numbers for the inertial end-corrections for slits, including the value for an infinitely thin plate, are in close agreement. This indicates that at high Shear numbers the plate thickness has a minor effect on the inertial end-correction. For a circular perforation, the finite limit value[23]

$\delta_{in,\Phi\to 0} = 0.41 d_p$ is found. For circular perforation, resistive and inertial end-corrections are of the same order of magnitude. It should be noted that for relevant porosities all end-corrections are of the order of L_{ref} (either b or d_p). For a given plate impedance, the normal incidence absorption of a microslit plate backed by a cavity with depth d can be calculated as shown, for example, in Zielinski *et al.*[5].

D. Modal expansion

In this subsection, the frictionless modal expansion proposed by Ingard[6] is used to derive an expression for the inertial end-correction. Given an arbitrary velocity profile at the end of the slit, it is possible to derive the inertial end-correction by matching this velocity profile with an expansion in modes of the confinement channel. Outgoing plane wave and evanescent transversal modes are considered. Kergomand and Garcia[20] discuss the convergence of the modal expansion. When using the rigid piston approximation in the slit the number of modes used in the channel should be of the order of the inverse of the porosity[18], $1/\Phi = a/b$. An expression of the inertial end-correction for low the Sh_b number is obtained by assuming a parabolic flow (see Sec. IIB) at the end of the slit. This is used as input for the frictionless modal expansion of the acoustic pressure in the channel. One finds:

$$\delta_{in} = \frac{5}{6}\sum_{n=1}^{\infty}\frac{3}{2n\pi}\left(\frac{a}{n\pi b}\right)^3\left\{4\cos^2(n\pi)\cdot\left[\cos\left(\frac{n\pi b}{a}\right)-\frac{a}{bn\pi}\sin\left(\frac{n\pi b}{a}\right)\right]\sin\left(\frac{n\pi b}{a}\right)\right\}. \quad (14)$$

A number of modes of the order of $N_m = 3(a/b)$ is sufficient to reach a reasonable accuracy.

For the asymmetric case, the influence of the position of the slit with respect to the wall is investigated. In Fig. 3, the transition from an asymmetric slit to a channel is displayed.

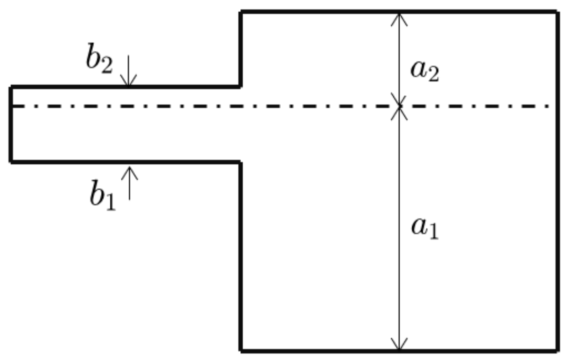

Figure 3: Geometry of the asymmetric slit of height $b = b_1 + b_2$ emerging in a channel of height $a = a_1 + a_2$.

The slit height is $b = b_1 + b_2$, the channel height is $a = a_1 + a_2$. The geometry is chosen such that the $(a/b) = (a_1/b_1) = (a_2/b_2)$. In the limit case of a slit sharing the flat wall with the channel, one has $a_2 = 0$ or $a_1 = 0$. The vertical positions of the slit edges (at $x = 0$) are $y_1 = a_1(1 - b/a)$ and $y_2 = a - a_2(1 - b/a)$. Assuming at the end of the slit a uniform acoustic velocity amplitude and expanding the amplitude of the pressure in frictionless modes in the channel one finds:

$$\delta_{in} = \sum_{n=1}^{\infty} \frac{2}{n\pi} \left\{ \frac{\left[\sin\left(\frac{n\pi y}{a}\right)\right]_{y_1}^{y_2}}{\frac{n\pi b}{a}} \right\}. \tag{15}$$

In the symmetric case $a_1 = a_2$ one finds the result of Ingard[6], where $n = 2m$. The sum is limited to even values of n. The influence of the position of the slit on the inertial end-correction is discussed in Sec. IV C.

E. Thin boundary layer approximation

For the high Sh_b range, the viscosity effects are concentrated in a thin boundary layer at the wall and do not impact the main, potential flow. The incompressible potential flow theory combined with the thin boundary layer approximation proposed by Morse and Ingard[8] can be used. A generalization of this model is presented by Berggren *et al.*[16]. In the present work, this approximation is used to investigate the end-corrections for smooth edges and asymmetric slit sharing the flat wall with the confinement channel. It is also used to explore the effect of viscous friction along the confinement channel walls(for the case of a partitioned back cavity). The smooth edge geometry is obtained using the conformal transformation introduced by Henrici[24] (Appendix A for details). An analytical solution is proposed in Appendix A for a smooth transition, providing a generalization of the results of Morse and Ingard[8] for sharp edges (Eq. 12-13).

In Fig. 4, a 2D slit of height b in $x < 0$ and a 2D channel of height $a > b$ in $x > 0$ are shown. The end of the uniform slit (point B in Fig. 4) is at $(x, y) = (-d, a - b)$, with d being the transition length. The uniform confinement channel begins at $x = 0$. The duct can be associated to a region in the complex $z-$plane by $z = x + iy$,with $i^2 = -1$ and

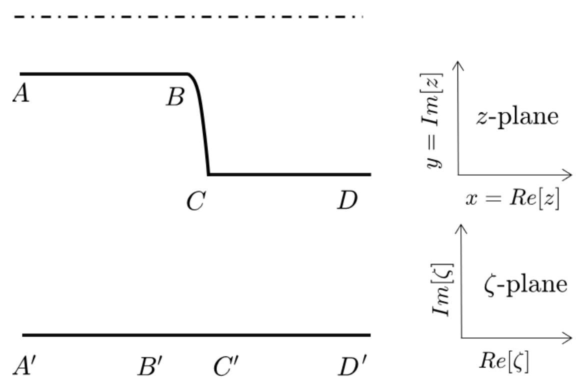

Figure 4: Henrici's transformation of half the channel with smooth transition from the slit to the channel in the physical plane $z = x + iy$ to the $\zeta-$plane. Coordinates of the points: $A(-\infty; (a+b)/2)$, $B(-d; (a-b)/2)$, $C(0,0)$, $D(\infty; 0)$.

spatial coordinates (x, y). Using conformal mapping, the flow region in the duct can be mapped into the upper half-plane in the complex $\zeta-$plane. The mapping of the contraction is a modified Schwarz-Christoffel transformation introduced by Henrici[24,25]. The differential form of Henrici's transformation is

$$\frac{dz}{d\zeta} = \zeta^{-1}\left[\alpha(\zeta-1)^{1/2} + \beta(\zeta-G^2)^{1/2}\right] \cdot (\zeta - G^2)^{-1/2}, \quad (16)$$

where α, β and G are parameters of the transformation depending on the slit and channel heights and on the transition length d. The parameters α and β are functions of the parameter G obtained numerically as the solution of a non-linear equation. Details are discussed in Appendix A. The equation for the sharp square edge transition is recovered for $d = 0$.

Using the thin boundary layer approximation one can find the real and imaginary part of the impedance of the transition Z_t and the corresponding inertial and resistive end-corrections. Formulas are provided in Appendix B.

A similar approach can be followed for a fully asymmetric slit, presented in Fig. 3. When $a_2 = 0$, the slit and the confinement channel share the flat wall. One has to add the dissipation of the flat wall, shared by the slit and the channel. This will be done by modifying the limits of integration when calculating the total dissipation along the walls (Appendix B). When the confinement channel walls are representing the influence of hydrodynamic interaction, the flow at the channel walls is frictionless. This can also be taken into account by simply modifying the integration limit when integrating to calculate the dissipated power. Details are in Appendix B. Parameters such as G are obtained numerically by solving a non-linear equation. The analytical solution for sharp edges can be used as an initial guess for small values of the transition length d. Then the parameter d can be increased using the previous value of G as an initial guess in an iteration process. Given G, in the symmetrical case, a fully analytical final solution is obtained. In other cases, a numerical integration remains to be carried out.

III. NUMERICAL MODEL

A. Uniform channel

Consider a uniform channel of height b and length t_p, with $t_p >> b$. The x-axis goes from $x = 0$ to $x = t_p$. The y-axis extends between the walls at $y = \pm b/2$. As stated in Sec. II A , the low He number approximation is made. The incompressible Linear Navier-Stokes equations for a 2D domain in a dimensionless form in the frequency domain are hereby presented:

$$\frac{\partial u^*}{\partial x^*} + \frac{\partial v^*}{\partial y^*} = 0, \tag{17}$$

$$iu^* = -\frac{\partial p^*}{\partial x^*} + \frac{1}{2Sh_b^2}\left(\frac{\partial^2 u^*}{\partial x^{*2}} + \frac{\partial^2 u^*}{\partial y^{*2}}\right), \tag{18}$$

$$iv^* = -\frac{\partial p^*}{\partial y^*} + \frac{1}{2Sh_b^2}\left(\frac{\partial^2 v^*}{\partial x^{*2}} + \frac{\partial^2 v^*}{\partial y^{*2}}\right), \tag{19}$$

with $x^* = x/b$ and $y* = y/b$. The dimensionless velocity (u^*, v^*) is $(u/b\omega, v/b\omega)$ and the dimensionless pressure is $p^* = p/(\rho(b\omega)^2)$. These equations are implemented in *Comsol Multiphysics* as user defined equations (PDE) and solved. At the inlet ($x^* = 0$) and at the outlet ($x^* = t_p/b$) of the domain the uniform pressure values are imposed: respectively, $p^*_{inlet} = 1$ and $p^*_{outlet} = 0$. At the walls ($y^* = y/b = \pm 1/2$) no-slip boundary conditions, $(u^*, v^*) = (0, 0)$ prevail. An unstructured mesh of quadratic triangular elements is used, with the finest mesh at the walls. The density of elements at the walls depends on the Sh_b number: the element sizes at the wall are $0.2/Sh_b$ or less, in order to accurately capture the viscous boundary layer. Several checks are performed to gain insight into the accuracy of the numerical simulations. Firstly, the computational domain length t_p is increased to exclude an influence of the channel length on the transition impedance. It appears that the quantity $U_L = Ut_p/t_{ref}$, with U being the flux in a cross-section of the channel and $t_{ref} = 6 * b$, is constant within a relative deviation of 10^{-5} for $0.5 < t_p/t_{ref} < 2$. Secondly, a mesh convergence study is performed and shows convergence to computer accuracy (10^{-13}). For this study, three additional meshes are used: one coarser and two finer meshes respectively with half, two, and four times the basic number of elements at the wall. To compare the results, the cross-sectional average velocity $< \widehat{u}^* >= \int_0^{b^*} \widehat{u}^* dy^*$ is used. Comsol[14] performs the integration element-wise using numeric quadrature of the 4^{th} order. The cross-sectional average velocity in the channel obtained with the numerical simulations shows a deviation of 10^{-4} from the analytical solution for the parallel flow in an infinitely long channel, discussed in Sec. II B.

B. Change in cross-section with sharp square edges

The set of equations 17-19 is used to study the channel in Fig. 5 presenting at $x^* = 0$ a sharp square edged transition from a uniform height b^* to a uniform height $a^* > b^*$. The channel extends from $x^* = -t_b^*$ to $x^* = t_a^*$, with $t_a^* = 6a/b$ and $t_b^* = t_a^*/2$.

The symmetry of the problem allows limiting the numerical domain to half the channel. For the inlet segment AF and outlet segment DE constant pressures are imposed, $p^*_{AF} = 1$ and $p^*_{DE} = 0$. At the segments AB and BC the no-slip boundary conditions are applied. At the segment EF (symmetry axis) a slip boundary conditions are implemented: $\partial u^*/\partial y^* = 0$

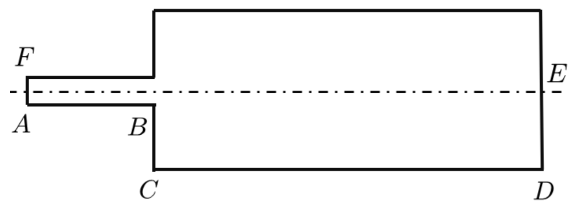

Figure 5: Geometry of a channel with the sudden transition from the slit of height b to the channel of height a.

and $v^* = 0$. The effect of the boundary condition at the walls is investigated. When considering a confinement channel due to hydrodynamic interaction, slip boundary condition is used on the segment CD. Far from the transition located at $x^* = 0$ the acoustic pressure is uniform in the cross-section and the amplitude of the pressure depends linearly on the position along the duct (parallel flow behavior). Assuming that for $-2a < x^* < -1a$: $\widehat{p}^{\,*}(x) = \widehat{A}x^* + \widehat{B}$ and for $3a < x^* < 5a$ one has: $\widehat{p}^{\,*}(x) = \widehat{C}x^* + \widehat{D}$. The complex constants can be determined by a linear fit of the pressure data obtained by numerical simulations for these regions far from the discontinuity. The linear fit gives a coefficient of determination[26] $1 - R^2 = 10^{-6}$. The impedance Z_t of the transition is determined by $Z_t = \frac{\widehat{B}-\widehat{D}}{\widehat{U}^*}$ with $\widehat{U}^*$ being the flux calculated in a generic section of the slit far from the discontinuity, defined as $\widehat{U}^* = w < \widehat{u}^* > b$. For a height ratio $a/b = 10$ and $Sh_b = 20$, in the proximity of the edges the maximum element size is $M_{el}/b = 2 \times 10^{-2}$ and the minimum is $m_{el}/b = 7 \times 10^{-4}$. The original mesh chosen for the standard calculations has a total of 13324 total elements, of which 804 are edge elements (at the walls). For a porosity $\Phi = b/a = 1/10$ at $Sh_b = 20$, numerical simulations show that the effect of the boundary condition at the lower wall of the channel is negligible. This confirms that the dissipation is mainly concentrated inside the slit and around the edges. In the assumption of locally incompressible flow, the volume flux along the duct axis is constant. This is verified numerically with a maximum relative deviation of 10^{-4}. The coefficients $\widehat{A}$ and $\widehat{C}$ of the linear fittings of $\widehat{p}^*$ can be compared to the theoretical values of the $\Delta\widehat{p}^*/t^*$ for the parallel flow in a long channel, respectively of height b and a. The discrepancy is in the order of 10^{-4}. The accuracy in the calculation of the volume flux is the limiting factor for the global accuracy of the numerical model.

IV. RESULTS

A. Symmetrical slit with sharp square edges

4.1.1 End-corrections at low and high Sh_b number

In this subsection, the end-corrections for a sharp square edged transition derived from the numerical simulations are compared with the analytical solutions proposed in Sec. II. An overview of the behavior of the end-corrections in the range $0.05 < Sh_b < 20$ is shown in Fig. 6. In Fig. 6 the behavior of δ_{in}/b and δ_{res}/b is shown as function of the Shear number and for several porosity. The Shear number range is divided into

- Low Sh_b range, $Sh_b < 0.6$,
- High Sh_b range, $0.6 < Sh_b < 20$.

The two ranges are discussed separately in the next subsections. For low Shear numbers, the inertial end-correction can be calculated using the oscillating parabolic flow approximation. For high Shear numbers the modal expansion of Ingard[6] and the thin boundary layer approximation of Morse and Ingard[8] are used. The inertial end-correction calculated by means of modal expansion with the parabolic flow approximation is about twice the value for uniform flow. In Fig. 7 the comparison between the numerical, the modal expansion, and thin boundary layer approximation, are shown as a function of the inverse of the porosity Φ. The numerical results are obtained for a $Sh_b = 0.05$ and for $Sh_b = 20$. At low Shear numbers, the Poiseuille flow approximation is used. At high Shear numbers, the thin boundary layer approximation and the plane piston model are compared. It appears that the parabolic (Poiseuille) flow approximation captures well the behavior of the inertial end-correction for $Sh_b = 0.05$, whereas the rigid piston and thin boundary layer models are in good agreement with the result for $Sh_b = 20$.

4.1.2 End-corrections at Low Sh_b number

For $Sh_b < 0.6$, the dimensionless inertial end-correction δ_{in}/b and the resistive end-correction δ_{res}/b are functions of the porosity and, to a much lesser degree, of the Sh_b number. The

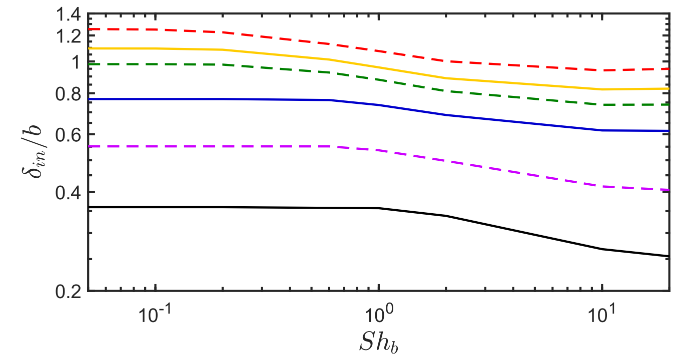

(a)

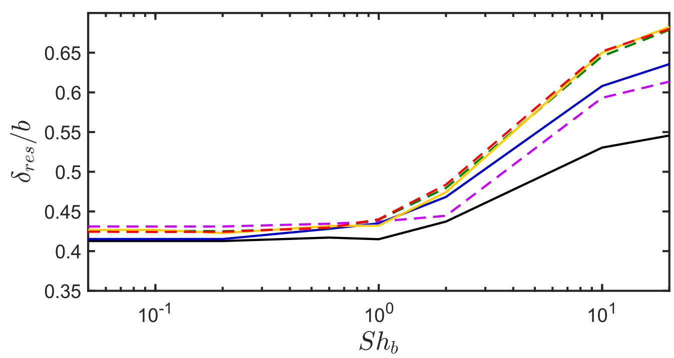

(b)

Figure 6: (Color online) Behavior of a) δ_{in}/b and b) δ_{res}/b from the numerical simulations as function of the Sh_b number for several porosities: —— $1/\Phi = 3$, - - - $1/\Phi = 5$, —— $1/\Phi = 10$, - - - $1/\Phi = 15$, —— $1/\Phi = 20$, - - - $1/\Phi = 30$.

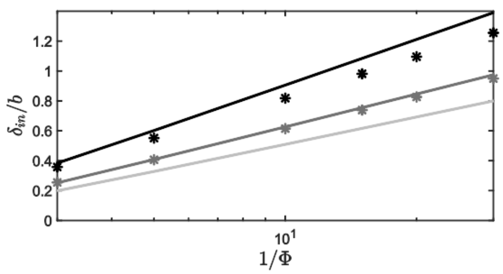

Figure 7: Comparison of inertial end-correction δ_{in} as functions of $1/\Phi$: — Parabolic flow approximation, — Uniform flow approximation[6]. — High the Sh_b number limit[8]. Stars refer to the results of numerical calculations for $*$ $Sh_b = 0.05$ and $*$ $Sh_b = 20$.

dependency of the end-corrections on Sh_b is therefore neglected for low Shear numbers. The dependency of δ_{res}/b on both porosity and the Sh_b number is negligible. The following fits are proposed:

$$\frac{\delta_{in,fit}}{b} = -2.17 + 2.18 * \left(\frac{1}{\Phi}\right)^{0.13}, \tag{20}$$

$$\frac{\delta_{res,fit}}{b} = 0.425, \tag{21}$$

for $Sh_b < 0.6$ and $3 < 1/\Phi < 30$. The coefficient of determination[26] $1 - R^2$ for δ_{in}/b is 0.997. The choice of the fit for δ_{res}/b results is a maximum underestimation of the actual value of 2.5%. The negligible effect of the porosity on δ_{res}/b indicates again that the dissipation is a local effect at the sharp edges. The comparison of the fits and the numerical data is provided[27,28].

4.1.3 End-corrections at high Sh_b number

In the region $0.6 < Sh_b < 20$ the deviations of δ_{in} and δ_{res} from the high Sh_b limits $\delta_{in,ref}$ and $\delta_{res,ref}$ (described in Sec. IIC and calculated for the same Shear number value as the numerical simulation), predicted by Morse and Ingard[8], have been obtained (see Appendix B). Proposed fits of the numerical results are:

$$\frac{\delta_{in}}{\delta_{in,ref}} - 1 = \frac{C_1}{C_2 + Sh_b}, \tag{22}$$

$$\frac{\delta_{res}}{\delta_{res,ref}} - 1 = \frac{C_3}{Sh_b * (C_4 + Sh_b)}, \tag{23}$$

$$\text{with } C_i = D_{i,1} + D_{i,2} \cdot (\Phi)\,. \tag{24}$$

From Eq. 24 appears that the coefficients C_i are linear functions of the porosity. Table 1 provides the values of the coefficients $D_{i,j}$.

Table 1: Values of the coefficients for the fitting in the range $0.6 < Sh_b < 20$.

	C_1	C_2	C_3	C_4
First coefficient $D_{i,1}$	0.52	1.27	5.19	1.69
Second coefficient $D_{i,2}$	9.34	7.45	28.74	3.97

In Fig. 6a and 6b both the inertial and resistive dimensionless end-corrections show a dependency on the porosity that becomes less important for decreasing porosity. This behavior is more noticeable for $\delta_{res}/\delta_{res,ref}$. In Fig. 8a the linear approximations of the coefficients C_1

and C_2 for the inertial end correction are compared with the actual values. In Fig. 8b the results for C_3 and C_4 for the resistance are presented. The average adjusted coefficients of

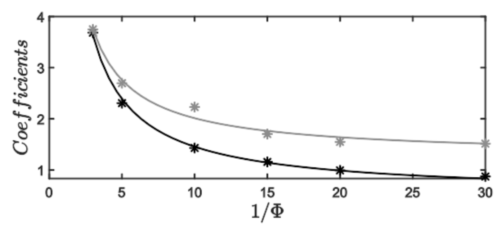

(a)

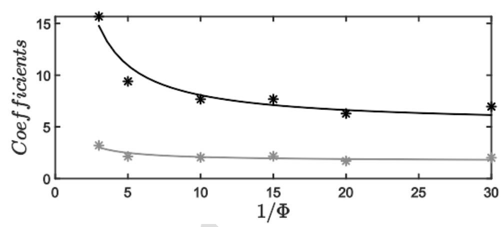

(b)

Figure 8: Comparison of the coefficients C_i of the fitting of the inertial and resistive end-corrections as function of the porosity Φ in the range $0.6 < Sh_b < 20$. In a) — C_1 and — C_2. In b) — C_3 and — C_4. In both, asterisks refer to the numerical data and solid lines are referred to the results of the fitting process.

determination[26] $1 - R^2$ are 0.987 for the inertial term and 0.998 for the resistive term. It appears that both $\delta_{in}/\delta_{in,ref}$ and $\delta_{res}/\delta_{res,ref}$ are converging to the unit value for high Sh_b numbers. For higher Sh_b numbers, some additional calculations are carried out for a typical porosity $1/\Phi = 10$. At $Sh_b = 100$, one has $\delta_{in}/\delta_{in,ref} = 1.0116$ and $\delta_{res}/\delta_{res,ref} = 0.9465$. At $Sh_b = 200$, $\delta_{in}/\delta_{in,ref} = 1.0061$ and $\delta_{res}/\delta_{res,ref} = 0.996$. This confirms the validity of the thin boundary layer approximation for sharp square edges. The effect of the boundary condition (slip or no-slip) on the channel walls is investigated for a typical porosity $1/\Phi = 10$ with $Sh_b = 2$ and $Sh_b = 20$. Numerical simulations for $1/\Phi = 10$ show that the introduction of a no-slip boundary condition at the walls of the confinement channel has a negligible effect on the results. For $Sh_b = 2$, one finds a ratio $\delta_{res,no-slip}/\delta_{res,slip} = 1.032$. For $Sh_b = 20$, $\delta_{res,no-slip}/\delta_{res,slip} = 1.044$. Using the thin boundary layer theory, for high Sh_b one finds $\delta_{res,no-slip}/\delta_{res,slip} = 1.041$, in agreement with numerical results. One expects that this ratio increases for increasing porosity. For an extremely large porosity $1/\Phi = 3$, one finds a ratio $\delta_{res,no-slip}/\delta_{res,slip} = 1.185$. One can conclude that the inertial end-correction is determined by the porosity. The porosity has a modest effect on the resistive end-correction. The negligible effect of the no-slip boundary condition in the channel suggests that, for $\Phi = 0.1$, dissipation is mainly concentrated around the edges. The comparison of the fits and the numerical data is provided[29,30].

B. Symmetric slit with smooth edges

Consider a slit of height b with rounded edges of radius r placed symmetrically with respect to a channel of height a. The results of incompressible LNS simulations are compared to the high Shear numbers approximation for a smooth transition discussed in Sec. II E with the shape determined by the transformation of Henrici[24]. Experimental and numerical data for a circular perforation obtained for a 45° chamfered circular perforation by Temiz *et al.*[13] are also displayed. The reference length L_{ref} is introduced. For the round edges $L_{ref} = r$ is the radius of curvature of the rounded edge. For Henrici's transformation, $L_{ref} = d$ is the transition length. For chamfered, $L_{ref} = c_{ch}$ is the chamfer length. It appears that the transition length d well approximates the radius r of an equivalent rounded edge for $d/b < 1$. In Fig. 9, $\delta_{in,round}/\delta_{in,sharp}$ and $\delta_{res,round}/\delta_{res,sharp}$ are displayed as function of L_{ref}/b. Numerical results for a slit with a height ratio of $a/b = 10$ are shown for: 1) rounded edges at several Sh_b numbers ($Sh_b = 0.2, 2, 20$), 2) chamfered edges for $c_{ch} = 0.5b$ at $Sh_b = 20$, 3) Henrici's geometry for $Sh_b = 20, 200$. The analytical potential solution for smooth edges is validated by the LNSE numerical simulations for Henrici's geometry at high Shear numbers. In Fig. 9a, for the inertial end-correction the analytical solution well approximates the numerical results for a rounded edge. The 2D planar result for the 45° chamfered edge is relatively far from the analytical and numerical results for a smooth transition. In Fig. 9b, for the resistive end-correction the analytical solution provides a good approximation for high Sh_b numbers, both for a round edge and for a chamfered edge. It is interesting to note that the resistive end-correction becomes negative for L_{ref}/b of order unity. For comparison, the influence of chamfer on circular perforations[13] is also displayed in Fig. 9. In Fig. 10a and 10b, $\delta_{in,round}/\delta_{in,sharp}$ and $\delta_{res,round}/\delta_{res,sharp}$ are shown for height ratios a/b relevant in MSPs. The inertial end-correction shows a dependency on a/b that increases with the increase of the ratio L_{ref}/b. The resistive end-correction shows a much more modest dependency on the porosity than the inertial end-correction, as already observed for sharp edges. Rounded edges and chamfered edges have a similar effect on the end-correction, for a small radius of curvature of the edge compared to the slit height *b*. The effect of rounded edges on a slit is similar to the effect of a chamfered edge for circular perforations. In conclusion, it appears that a fair estimation of the edge geometry is necessary to obtain meaningful estimations of the end-correction for both slits and circular perforations.

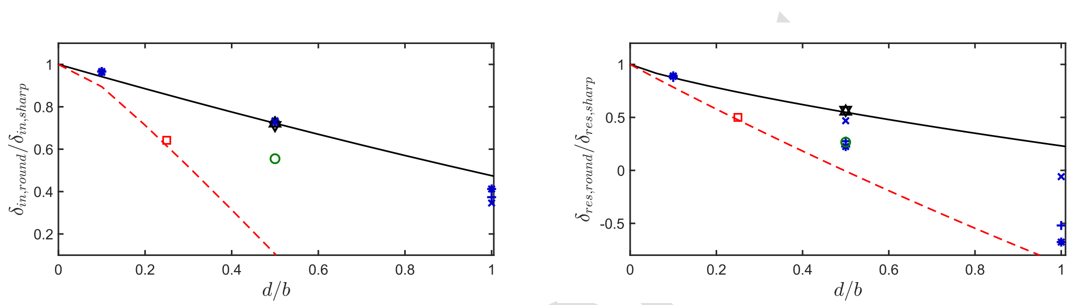

(a) (b)

Figure 9: (Color online) Comparison of the high Sh_b number approximation for a smooth transition with numerical results for several ratios L_{ref}/b for a)$\delta_{in,round}/\delta_{in,sharp}$ and b)$\delta_{res,round}/\delta_{res,sharp}$ for several Sh_b numbers: — Slit with smooth transition, $*$ Slit with rounded edges for $Sh_b = 0.2$, $+$ Slit with rounded edges for $Sh_b = 2$, $\times$ Slit with rounded edges for $Sh_b = 20$, $\bigtriangledown$ Slit with Henrici's transition for $Sh_b = 20$, $\triangle$ Henrici's transition for $Sh_b = 200$, $\bigcirc$ Chamfered edge for $Sh_b = 20$, - - - Fit of numerical results and $\square$ Experimental result for circular perforations of Temiz *et al.*[13].

C. Asymmetric slit

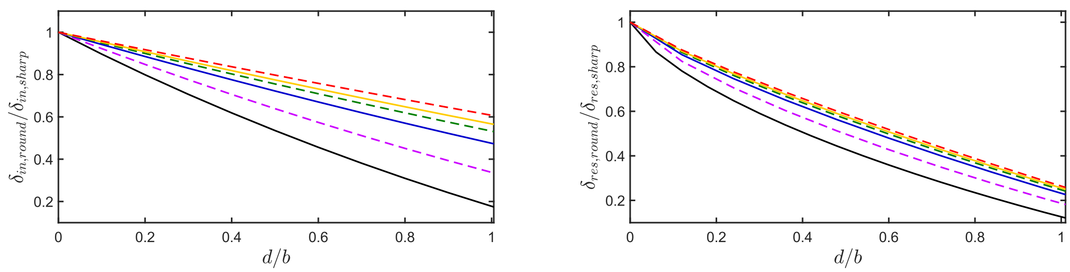

(a) (b)

Figure 10: (Color online) Behavior of a) $\delta_{in,round}/\delta_{in,sharp}$ and b) $\delta_{res,round}/\delta_{res,sharp}$ as function of the edge rounding L_{ref}/b for several $1/\Phi = a/b$: — $1/\Phi = 3$, - - - $1/\Phi = 5$, — $1/\Phi = 10$, - - - $1/\Phi = 15$, — $1/\Phi = 20$, - - - $1/\Phi = 30$.

In this section results for asymmetric slits are discussed. The position of the slit is determined using the distances a_1 and a_2 defined in Fig. 3. The inertial end-correction is calculated for high Sh_b numbers, using the modal expansion method of Ingard[6] presented in Sec. II D. In the extreme case that $a_2 = 0$, the high Sh_b number limit of Morse and Ingard[8] can be used to calculate both the inertial and the resistive end-corrections.

In Fig. 11 the ratio of the inertial end-corrections for the asymmetric case ($\delta_{in,asym}$) and the symmetric case ($\delta_{in,sym}$) is displayed as function of a_2/a_1 for several height ratios a/b, with $a = a_1 + a_2$. The value of a_2/a_1 where the effect of the position has a significant effect decreases with the increase of a/b. It appears that for a slit positioned at the wall ($a_2 = 0$), the inertial end-correction is, as expected, double the value for the symmetric

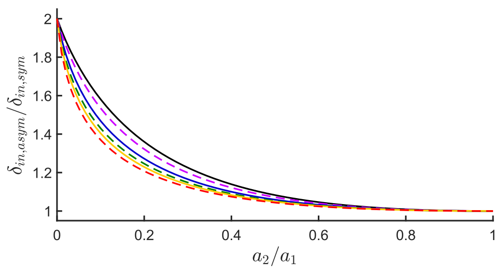

Figure 11: (Color online) Analytical results for the inertial end-correction obtained by means of modal expansion for an asymmetric slit for several $1/\Phi$: — $1/\Phi = 3$, - - - $1/\Phi = 5$, — $1/\Phi = 10$, - - - $1/\Phi = 15$, — $1/\Phi = 20$, - - - $1/\Phi = 30$.

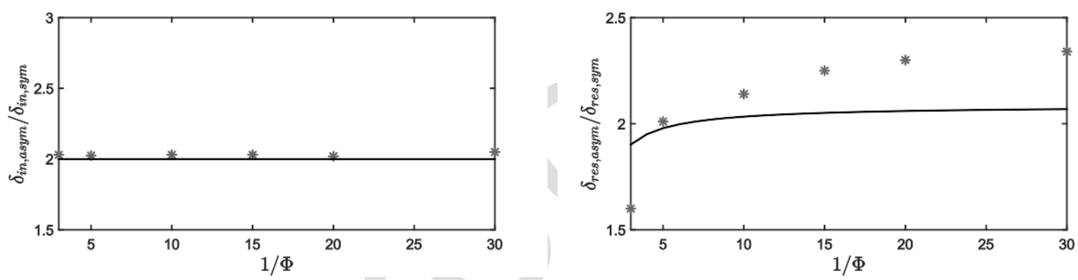

(a) (b)

Figure 12: Comparison of the numerical simulations ($*$) for $Sh_b = 20$ and potential flow theory (—) results as function of a/b for a) $\delta_{in,asym}/\delta_{in,sym}$ and b)$\delta_{res,asym}/\delta_{res,sym}$.

case, for all the ratios a/b. Numerical calculations are performed for a slit positioned at the wall and compared to the analytical results. In Fig. 12, for $Sh_b = 20$ the end-corrections for an asymmetric slit ($a_2 = 0$) as function of the height ratio a/b are plotted using the corresponding values (same Sh_b number) for a symmetric slit as a reference. The inertial end-correction is double the value for the symmetric slit. The resistive end correction instead increases for decreasing porosity $\Phi = b/a$. It approaches the asymptotic value of $\delta_{res,asym} = 2.3\delta_{res,sym}$. This asymptotic value reduces for increasing Sh_b approaching the analytical value for very high Shear numbers. Considering the common wall as a mirror, the flow corresponds to that in a slit with double width $2b$ placed symmetrically with respect to a channel of width $2a$. This explains the behavior of the inertial end-correction. For the resistive end-correction, the dissipation occurs in a small region around the edge. This region can be addressed as the dissipation region. When keeping the flow velocity in the slit constant, but doubling the slit and channel height, one increases the dissipation region length by a factor 2. The resulting resistive end-correction doubles. In practice, the end-correction increase is larger (15%) than the factor 2 because one has to account for an additional dissipation along the flat wall common to the slit and the channel. The deviation at $a/b = 30$ for the resistive end-correction indicates that the thin boundary layer limit is not yet reached for $Sh_b = 20$. This was also observed for the symmetrical case. In conclusion, it appears that the influence of the position on the end-corrections cannot be neglected for positions of the slit with respect to the channel of the order of magnitude of the slit height.

D. Finite thickness plate with sharp square edges

In Fig. 13a and 13b the deviations of the inertial and resistive end-correction for a finite thickness are compared with the transition between a very long slit and the confinement channel discussed in the previous sections. In the range of interest, the deviation lays within 10% and 5% accuracy, respectively for the inertial and the resistive end-correction. $\delta_{res,plate}$ shows a negligible dependency on t_p/b with respect to the dependency on the Sh_b number. From this study, one can state that for practical purposes the influence of the thickness of the plate on the end-corrections can be neglected.

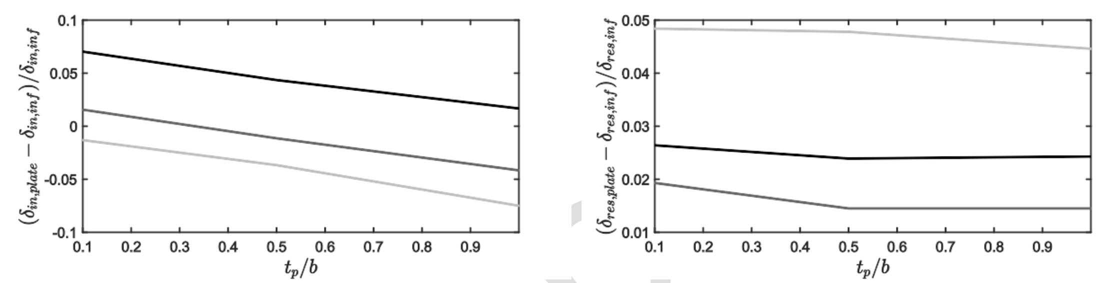

(a) (b)

Figure 13: Deviation of a) $(\delta_{in,plate}$ and b)$(\delta_{res,plate}$ from the semi-infinite slit as function of the ratio t/b for: — $Sh_b = 0.2$, — $Sh_b = 2$ and — $Sh_b = 20$.

V. CONCLUSIONS

In typical microslit plates (MSPs) the acoustic end-corrections and the plate thickness are both of the order of the slit width. Hence an accurate prediction of the end-corrections is needed for the design of MSPs. This study combines two-dimensional analytical and numerical solutions of the incompressible Linearized Navier-Stokes equations to investigate the acoustic behavior of microslit absorbers (MSAs and MSPs). A single slit of height b is studied as confined in a rectangular channel of height a determined by the porosity of the plate $\Phi = b/a$. The flow within the slit is assumed to be locally incompressible (low He numbers). Thermal effects are neglected. Focus is given to the frequency range of application for MSAs and resonant metamaterials. For sharp edges, numerical simulations demonstrate that for low Sh_b numbers a parabolic flow approximation provides a good approximation of the inertial end-correction, whereas the thin boundary layer approximation predicts both the end-corrections at high Sh_b numbers. The inertial end-correction of slits is strongly dependent on the porosity, showing a very different behavior compared to that of circular perforations. A striking result is that the ratio of the resistive end-correction and the slit height is weakly dependent on the porosity, independently of the Shear number. This indicates that viscous friction is a local phenomenon occurring near the edges. This is confirmed by the negligible influence of the no-slip boundary condition at the walls of the confinement channel, for $\Phi < 0.1$. The final prove is gathered in Sec. IV B where the effect of the edge geometry is discussed. The analytical model for a smooth transition provides a reasonable prediction for rounded and chamfered edges at high Sh_b numbers. These results demonstrate that, without information on the edge shape, an accurate prediction of the end-corrections is not possible. In Sec. IV C it is shown that the position of the slit becomes an important effect for distance from the wall in the order of the slit height b.

For the limit case of a slit sharing the wall with the channel, the inertial and resistive end-corrections are both approximately twice the values for a symmetrical slit. In Sec. IV D it is shown that, for $t_p > 0.1b$, the effect of the plate thickness on the end-corrections is negligible.

ACKOWLEDGMENTS

The authors acknowledge prof. S. Rienstra for the contributions in conformal mapping and complex function theory. This work is part of the Marie Skłodowska-Curie Initial Training Network Pollution Know-How and Abatement (POLKA). We gratefully acknowledge the financial support from the European Commission under call H2020-MSCA-ITN-2018.

APPENDIX A: TRANSFORMATION OF HENRICI

In this appendix the high Sh_b limit theory is described for the smooth and asymmetric transitions presented in Sec. II E. The duct can be associated to a region in the complex $z-$plane by $z = x + iy$, with $i^2 = -1$ where (x, y) are the coordinates in the physical plane. Using conformal mapping, the flow region in the duct in the complex $z-$plane is mapped into the upper half-plane in the complex $\zeta-$plane The transformation of Henrici[24] is used to derive the results for a smooth transition from a slit of height b to a channel of height a. The geometry is presented in Fig. 4. The integral form of the transformation proposed by Henrici[24] is:

$$z = \alpha\left[\ln\frac{1+\tau}{1-\tau} - \frac{1}{G}\ln\left(\frac{G+\tau}{G-\tau}\right)\right] + \beta\ln\left[\frac{\zeta}{G^2}\right]^{25}, \tag{25}$$

where τ is:

$$\tau = \sqrt{\frac{\zeta - G^2}{\zeta - 1}}. \tag{26}$$

The point far downstream of the transition A($(-\infty, a)$ can be mapped into point A'($\zeta = 0$), the start of the transition B($-d, a - b/2$) corresponds to B'($\zeta = 1$), the end of the transition C($0, 0$) corresponds to C'($\zeta = G^2$). The coefficients are related to parameter G by:

$$\alpha = \frac{a-b}{\pi}\left[\frac{G}{G-1}\right] \tag{27}$$

and

$$\beta = \frac{G\ b - a}{\pi(G-1)}. \tag{28}$$

The parameter G is found by solving the non-linear equation:

$$G = \frac{a}{b}\left[1 + \frac{\pi\ d}{2\ a\ln G}(G-1)\right]. \tag{29}$$

This equation can be solved by successive substitution for $\pi d\,(2b) < 2$ using $G_0 = a/b$ as initial guess. For $\pi d\,(2b) > 2$ the successive substitutions should be applied to:

$$G = \exp\left[\frac{\pi d}{2b}\left(\frac{G-1}{G-\frac{a}{b}}\right)\right], \tag{30}$$

using $G_0 = \exp\left(\frac{\pi d}{2b}\right)$. For sharp edges $d = 0$ and $G = a/b$. For an asymmetric slit positioned at the wall it is necessary to identify the point ζ_0 on the ζ-axes that corresponds to $z_0 = ia$ on the flat wall in the z-plane. ζ_0 is found by solving numerically the equation $z_0 = z(\zeta_0) = ia$.

This can be done for any value of the transition length d. Here, only the sharp edge ($d = 0$) is considered for the fully asymmetric slit position ($a_2 = 0$).

APPENDIX B: THIN BOUNDARY LAYER APPROXIMATION

The thin boundary layer method of Morse and Ingard[8] for the transition from a slit of height b to a channel a with sharp edges is extended to a smooth transition and to a fully asymmetric slit positioned at the wall ($a_2 = 0$). The inertial and resistive end-corrections can be found comparing the actual configuration with an ideal configuration. The ideal reference flow, used to define the end-corrections, has for $x > 0$ a uniform velocity u_a in the channel of height a and for $x < 0$ a uniform velocity $u_b = (a/b)u_a$. The potential flow far upstream is obtained by placing a volume source at the origin $\zeta = 0$ (far downstream the transition) with potential $\varphi = (au_a/\pi)\, ln(\zeta)$. The local flow velocity is the vector field $\vec{v}_{wall} = (u, v) = \nabla\varphi$. The linearized form of the frictionless equation of motion is

$$-\nabla p = \rho \frac{\partial \vec{v}}{\partial t}. \tag{31}$$

To compare the actual and the reference configurations two points in the transformed $\zeta-$plane are necessary. Choosing $\zeta_1 \to \infty$ and $\zeta_2 = 0$ corresponds to z_1 and z_2 respectively far upstream and far downstream the transition. Integrating Eq. 31 between $z_1 = (x_1; y_1)$ and $z_2 = (x_2; y_2)$ with $x_1 > 0$ and $x_2 < 0$, one has for a harmonic oscillating acoustic field:

$$\mathrm{i}\rho\omega(\varphi_2 - \varphi_1) = p_1 - p_2, \tag{32}$$

with $\varphi = \int \vec{v} \cdot d\vec{z}$. If the flow velocity would remain uniform $(u_a, 0)$ for $x > 0$ and jump to $(u_b, 0)$ with $u_b = u_a a/b$ for $x < 0$, we would have:

$$(\varphi_2 - \varphi_1)_{ideal} = u_a \frac{a}{b} x_2 - u_a x_1. \tag{33}$$

The inertia $Im[Z_t]$ is given by:

$$Im[Z_t] = \frac{\rho\omega\Delta\varphi}{awu_a}, \tag{34}$$

Where $\Delta\varphi$ is defined as the difference $(\varphi_2 - \varphi_1)_{actual} - (\varphi_2 - \varphi_1)_{ideal}$. Choosing real values ζ_1 and ζ_2, so that the values of z_1 and z_2 are far from the origin of the axis, one has:

$$Im[Z_t] = \frac{\rho\omega}{wb} \left[\frac{b}{\pi} \ln\left(\frac{\zeta_2}{\zeta_1}\right) - Re(z_2) + \frac{b}{a} Re(z_1) \right]. \tag{35}$$

For $\zeta_1 \to \infty$ and $\zeta_2 \to 0$ in Eq. 25 and Eq. 26 we can expand at the first order τ and obtain an expression for z_1 and z_2 to substitute in Eq. 35. One arrives at Eq. 36. For $d = 0$ this expression recovers the result of Morse and Ingard[8].

$$\begin{aligned} Im[Z_t] = \frac{\rho\omega}{\pi w} \Bigg\{ & \frac{(a-b)^2}{2ab} \ln\left(\frac{G+1}{G-1}\right) + \frac{a-b}{b(G-1)} \\ & \cdot \left[\frac{Gb+a}{2a} \ln\left(\frac{(1+G)^2}{4G^2}\right) \right] + \ln G \Bigg\}. \end{aligned} \tag{36}$$

Using Eq. 10 one can find the inertial end-correction. The additional dissipation due to the transition can be derived integrating along the wall the dissipation per unit surface presented in Sec. II B for the actual and the reference configuration. It should be noted that the actual configuration and the ideal configuration should be combined to obtain converging integrals.

In terms of potential the velocity at the wall is:

$$|\widehat{u}_{tan}|^2 = \left|\frac{d\varphi}{dz}\right|^2 = \left|\frac{d\varphi}{d\zeta}\right|^2 \left|\frac{d\zeta}{dz}\right|^2. \tag{37}$$

The power dissipated at the junction compared to an ideal configuration is:

$$\bar{P}_W = \frac{1}{2\delta_v}\eta w\Bigg[\int_{\zeta_2}^{\zeta_0}\left(\left|\frac{d\varphi}{d\zeta}\right|^2 \frac{d\zeta}{dz} - u_a^2 * \left(\frac{a}{b}\right)^2 Re\left[\frac{dz}{d\zeta}\right]\right) d\zeta + \int_{\zeta_0}^{\zeta_1}\left(\left|\frac{d\varphi}{d\zeta}\right|^2 \frac{d\zeta}{dz} - u_a^2 Re\left[\frac{dz}{d\zeta}\right]\right) d\zeta\Bigg], \tag{38}$$

where for a symmetric slit $\zeta_1 \to \infty$, $\zeta_2 \to 0$ and ζ_0 corresponds to $z = 0$ and it is found from $\zeta_0 = G^2$. The second integral in Eq. 38 contains the effect of the dissipation in the channel. For a slip boundary condition prevailing in a confinement channel resulting from hydrodynamic interactions, one can take $\zeta_1 \to \zeta_0$ and calculate the dissipation using only the first integral. These integrals can be solved by numerical integration with standard numerical solvers. The resistance of the discontinuity can be defined as Morse and Ingard[8]:

$$Re[Z_t] = \frac{2\bar{P}_W}{(aw|u_a|)^2}. \tag{39}$$

Solving analytically the integrals for the symmetric smooth-edged configuration with friction at the channel walls leads to an approximated expression for $Re[Z_t]$,

$$Re[Z_t] = \frac{\rho\omega}{2Sh_b w}\frac{(G-1)}{G(a-b)}\Bigg\{(G-1)\Bigg[\frac{(G+1)}{\pi(G-1)}\left(\frac{G^2(a-b)^2}{b^2(G+1)(G-1)^2} - 1\right) \cdot \ln\left(\frac{G+1}{G-1}\right) + 1\Bigg] - \frac{2DG^2}{\pi}\ln(G)\Bigg\}, \tag{40}$$

with $D = \frac{Gb-a}{G(a-b)}$. This formula is valid for $\Phi > 1/2$. For $d = 0$ one recovers $D = 0$ and $G = 1/\Phi$ and one obtains an approximation of the result of Morse and Ingard[8], with an error of the order of 10^{-4} for a porosity $\Phi = 1/10$. This error decreases for decreasing porosities. Using Eq. 11 one can find the resistive end-correction.

For an asymmetric slit, the dissipation of the transition, in this case, is the sum of the dissipation of the wall with an edge and the dissipation at the opposite flat wall. The same integrals can be solved by changing the integration to $\zeta_1 \to \infty$, $\zeta_2 \to -\infty$ and ζ_0 can be found solving numerically the equation $z_0 = z(\zeta_0) = ia$, using Henrici's transformation formula (Eq. 25).

REFERENCES

1. Maa, D.-Y. (**2000**). "Theory of microslit absorbers," Acta Acustica **25**(6), 481–485.

2. Kristiansen, U. R., and Vigran, T. E. (**1994**). "On the design of resonant absorbers using a slotted plate," Applied Acoustics **43**(1), 39–48.

3. Randeberg, R. (**2002**). "Adjustable slitted panel absorber," Acta Acustica united with Acustica **88**(4), 507–512.

4. Ruiz, H., Claeys, C., Deckers, E., and Desmet, W. (**2016**). "Numerical and experimental study of the effect of microslits on the normal absorption of structural metamaterials," Mechanical Systems and Signal Processing **70**, 904–918.

5. Zieliński, T. G., Chevillotte, F., and Deckers, E. (**2019**). "Sound absorption of plates with micro-slits backed with air cavities: Analytical estimations, numerical calculations and experimental validations," Applied Acoustics **146**, 261–279.

6. Ingard, U. (**1953**). "On the theory and design of acoustic resonators," The Journal of the acoustical society of America **25**(6), 1037–1061.

7. Jaouen, L., and Chevillotte, F. (**2018**). "Length correction of 2d discontinuities or perforations at large wavelengths and for linear acoustics," Acta Acustica united with Acustica **104**(2), 243–250.

8. Morse, P. M., and Ingard, K. U. (**1986**). *Theoretical acoustics* (Princeton University press).

9. Vigran, T. (**2014**). "The acoustic properties of panels with rectangular apertures," The Journal of the Acoustical Society of America **135**(5), 2777–2784.

10. Billard, R., Tissot, G., Gabard, G., and Versaevel, M. (**2021**). "Numerical simulations of perforated plate liners: Analysis of the visco-thermal dissipation mechanisms," The Journal of the Acoustical Society of America **149**(1), 16–27.

11. Ruiz, H., Cobo, P., and Jacobsen, F. (**2011**). "Optimization of multiple-layer microperforated panels by simulated annealing," Applied Acoustics **72**(10), 772–776.

12. Cobo, P., de la Colina, C., and Simón, F. (**2020**). "On the modelling of microslit panel absorbers," Applied Acoustics **159**, 107118.

13. Temiz, M. A., Lopez Arteaga, I., Efraimsson, G., Åbom, M., and Hirschberg, A. (**2015**). "The influence of edge geometry on end-correction coefficients in micro perforated plates," The Journal of the Acoustical Society of America **138**(6), 3668–3677.

14. Comsol (**v.5.5.**). "Comsol multiphysics®," COMSOL AB, Stockholm, Sweden. www.comsol.com .

15. Landau, L., and Lifshitz, E. (**1987**). "Course of theoretical physics, vol. 6: Fluid mechanics 2, nd, ed" .

16. Berggren, M., Bernland, A., and Noreland, D. (**2018**). "Acoustic boundary layers as boundary conditions," Journal of Computational Physics **371**, 633–650.

17. Lighthill, M. J., (**2001**). *Waves in fluids* (Cambridge university press).

18. Rienstra, S. W., and Hirschberg, A. (**2004**). "An introduction to acoustics," Eindhoven University of Technology **18**, 19.

19. Lesser, M., and Lewis, J. (**1972**). "Applications of matched asymptotic expansion methods to acoustics. ii. the open-ended duct," The Journal of the Acoustical Society of America **52**(5B), 1406–1410.

20. Kergomard, J., and Garcia, A. (**1987**). "Simple discontinuities in acoustic waveguides at low frequencies: critical analysis and formulae," Journal of Sound and Vibration **114**(3), 465–479.

21. Fok, V. (**1941**). "Teoreticheskoe issledovanie provodimosti kruglogo otverstiya v peregorodke, postavlennoi poperek truby (theoretical study of the conductance of a circular hole in a partition across a tube)," Doklady Akademii Nauk SSSR (Soviet Physics Doklady) **31**(9), 875–882.

22. Naderyan, V., Raspet, R., Hickey, C. J., and Mohammadi, M. (**2019**). "Acoustic end corrections for micro-perforated plates," The Journal of the Acoustical Society of America **146**(4), EL399–EL404.

23. Maa, D.-Y. (**1998**). "Potential of microperforated panel absorber," the Journal of the Acoustical Society of America **104**(5), 2861–2866.

24. Henrici, P. (**1974**). *Applied and computational complex analysis, Volume I* (John Wiley & Sons).

25. Hirschberg, L., Schuller, T., Collinet, J., Schram, C., and Hirschberg, A. (**2018**). "Analytical model for the prediction of pulsations in a cold-gas scale-model of a solid rocket motor," Journal of Sound and Vibration **419**, 452–468.

26. Glantz, S., and Slinker, B. (**2001**). *Primer of Applied Regression & Analysis of Variance, ed* (McGraw-Hill, Inc., New York).

27. See supplementary material at [URL will be inserted by AIP] for comparison of the numerical data with the proposed fits in the low Shear number range. The color scale is the same used in Fig. 6.

28. See supplementary material at [URL will be inserted by AIP] for comparison of the numerical data with the proposed fits in the low Shear number range. The color scale is the same used in Fig. 6.

29. See supplementary material at [URL will be inserted by AIP] for comparison of the numerical data with the proposed fits in the low Shear number range. The color scale is the same used in Fig. 6.

30. See supplementary material at [URL will be inserted by AIP] for comparison of the numerical data with the proposed fits in the low Shear number range. The color scale is the same used in Fig. 6.